Science Advances
AAAS

advances.sciencemag.org/cgi/content/full/6/9/eaay6898/DC1

Supplementary Materials for

The Moon's farside shallow subsurface structure unveiled by Chang'E-4 Lunar Penetrating Radar

Chunlai Li, Yan Su*, Elena Pettinelli*, Shuguo Xing*, Chunyu Ding, Jianjun Liu, Xin Ren, Sebastian E. Lauro, Francesco Soldovieri, Xingguo Zeng, Xingye Gao, Wangli Chen, Shun Dai, Dawei Liu, Guangliang Zhang, Wei Zuo, Weibin Wen, Zhoubin Zhang, Xiaoxia Zhang, Hongbo Zhang

*Corresponding author. Email: suyan@nao.cas.cn (Y.S.); pettinelli@fis.uniroma3.it (E.P.); xingsg@nao.cas.cn (S.X.)

Published 26 February 2020, *Sci. Adv.* **6**, eaay6898 (2020)
DOI: 10.1126/sciadv.aay6898

This PDF file includes:

Fig. S1. CE-4 landing site. Optical image at the CE-4 landing site taken by the Panoramic Camera (PCAM) on Yutu-2 rover, showing the paucity of large rocks and boulders on the surface around the investigated area.

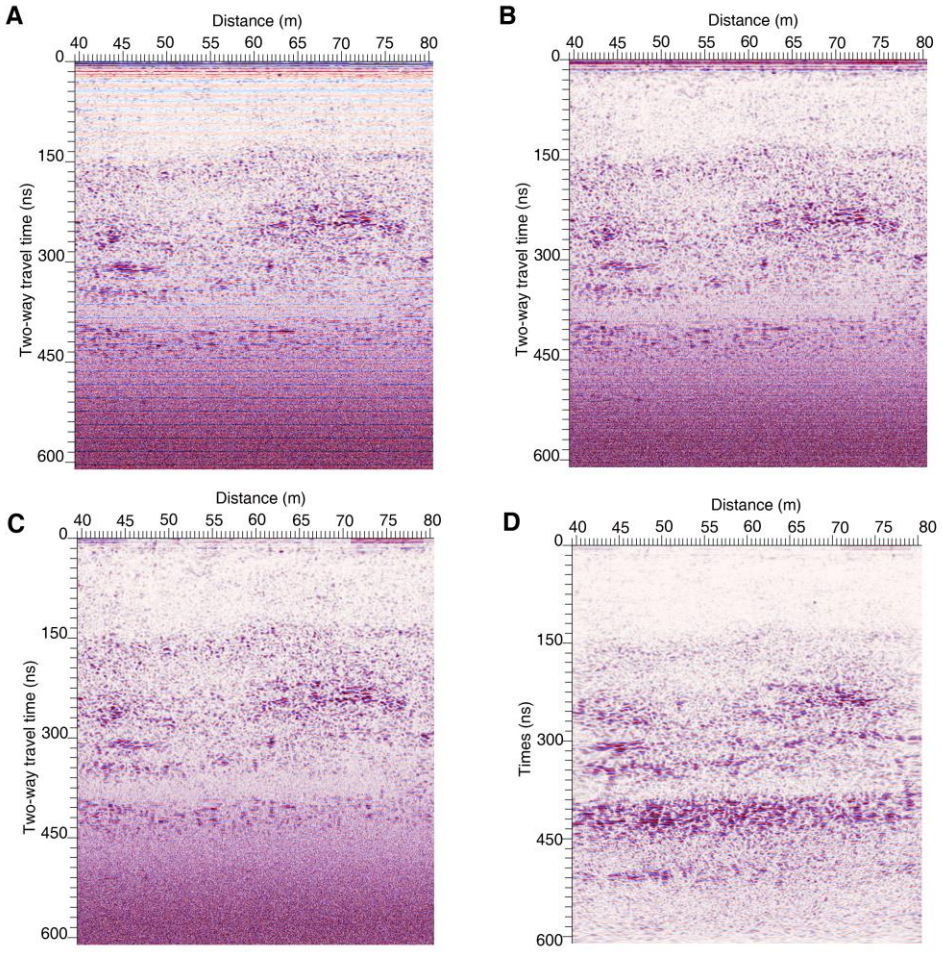

Fig. S2. Data processing procedure of LPR high frequency. (A) Raw data. **(B)** After Dewow filter applied. **(C)** After Dewow+background subtraction applied. **(D)** After migration applied. All figures are plotted with a SEC gain (starting point 0.01, attenuation 0.5, maximum gain value 50, apart for panel D that has attenuation 0.8 and maximum gain 100). Note that panels (A-D) only illustrate the central part of the section to better show the effect of the processing, whereas the entire radargram (106 m) is depicted in the main text.

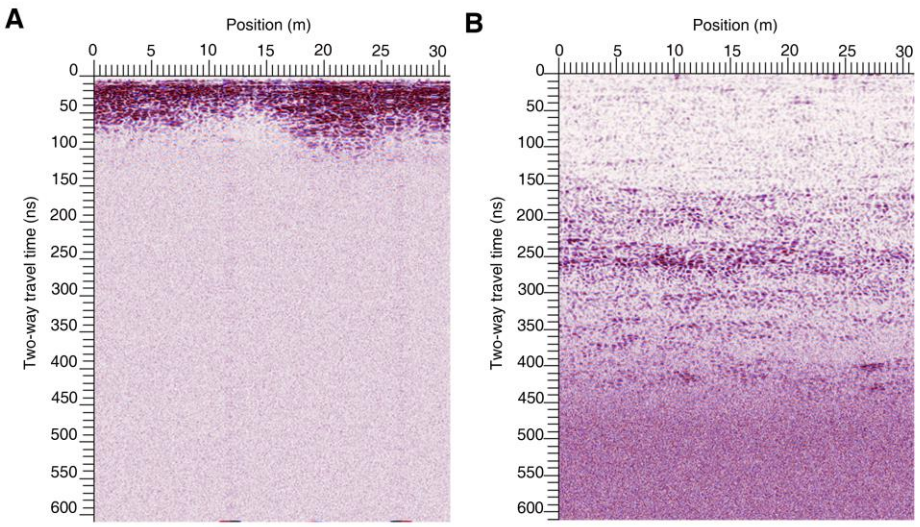

Fig. S3. Comparison of high-frequency LPR data between CE-3 and CE-4. (A) First 30 m collected by CE-3 at the Zi Wei crater landing site and **(B)** by CE-4 at Von Kármán crater landing site. Both sections have the same processing applied, that is, Dewow and background subtraction and are plotted with a SEC gain (starting point 0.01, attenuation 0.5, maximum gain value 50).

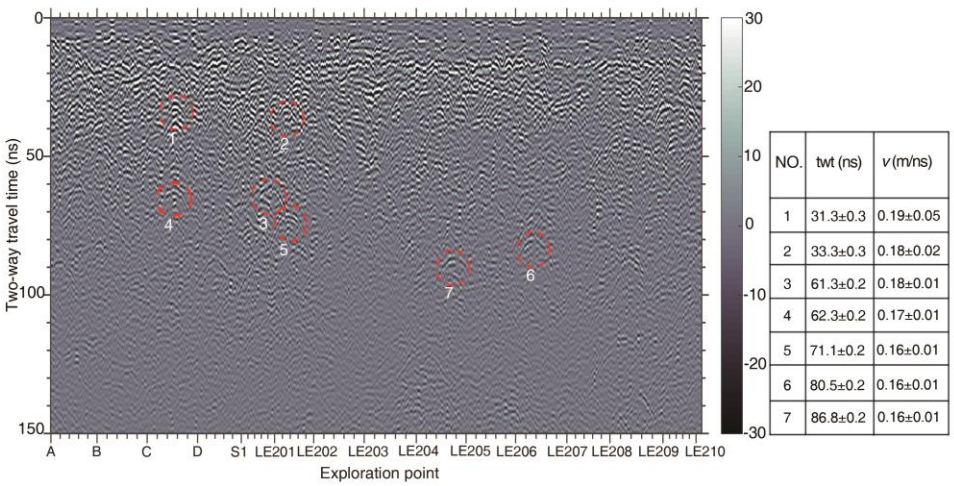

NO.	twt (ns)	*v* (m/ns)
1	31.3±0.3	0.19±0.05
2	33.3±0.3	0.18±0.02
3	61.3±0.2	0.18±0.01
4	62.3±0.2	0.17±0.01
5	71.1±0.2	0.16±0.01
6	80.5±0.2	0.16±0.01
7	86.8±0.2	0.16±0.01

Fig. S4. Velocity estimation using point targets. Location of the hyperbolas used to calculate the average electromagnetic wave velocities (left image), two-way travel time (twt) and velocity (*v*) for the different hyperbolas (right table).

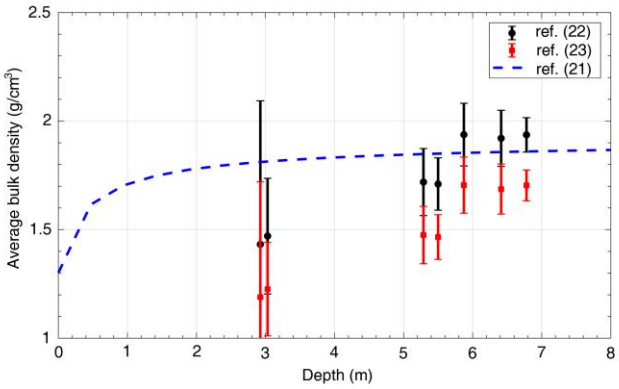

Fig. S5. Bulk density versus depth in the first 8 m. Average bulk density computed using equation (1) (black dots) and equation (2) (red dots) as a function of depth, based on the velocity analysis. Blue line represents the average bulk density according to ref.*(21)*.

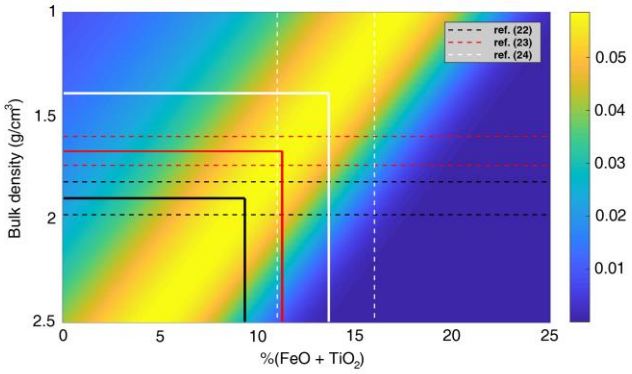

Fig. S6. Joint probability density function of loss tangent as a function of bulk density and oxide content. White dash lines indicate ($FeO+TiO_2$) range measured by Kaguya MI at CE-4 landing site. Red and black dashed lines indicate the bulk density range calculated using equation (2) and (1), respectively. Solid lines give the relation between bulk density and oxides content for the maximum value of the probability density function, that is, $\tan\delta = 5\times10^{-3}$.

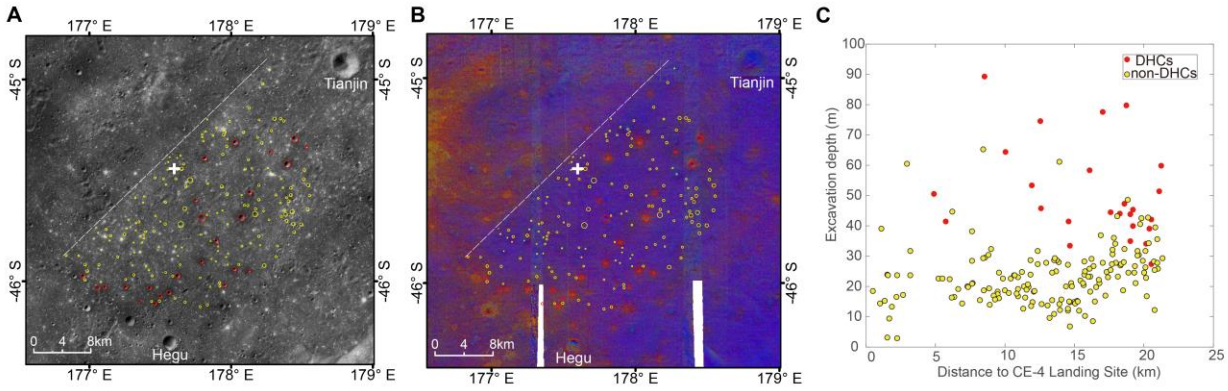

Fig. S7. Estimation of the ejecta thickness using DHCs and non-DHCs. (A) The distribution of DHCs and non-DHCs over the CE-4 landing region. The red circles represent DHCs that have penetrated the ejecta layer, and the yellow circles are non-DHCs that did not penetrate the ejecta layer. The white cross represents the CE-4 landing site. The white dashed line shows the boundary for crater counting, and DHCs can be found only in the right region. The background map is CE-2 Digital Orthophoto Map (DOM) data with a spatial resolution of 7 m. The mare basalts appear dark, whereas the ejecta appear bright. **(B)** False color image of the Kaguya Multiband Imager (MI) showing surface composition of the landing site (R represents FeO content, G represents high-calcium pyroxene content, and B represents plagioclase content). The mare basalts appear as red-yellow-green, and the ejecta are blue-purple in color. **(C)** Excavation depth as a function of distance from the CE-4 landing site estimated for DHCs (red dots) and non-DHCs (yellow dots).

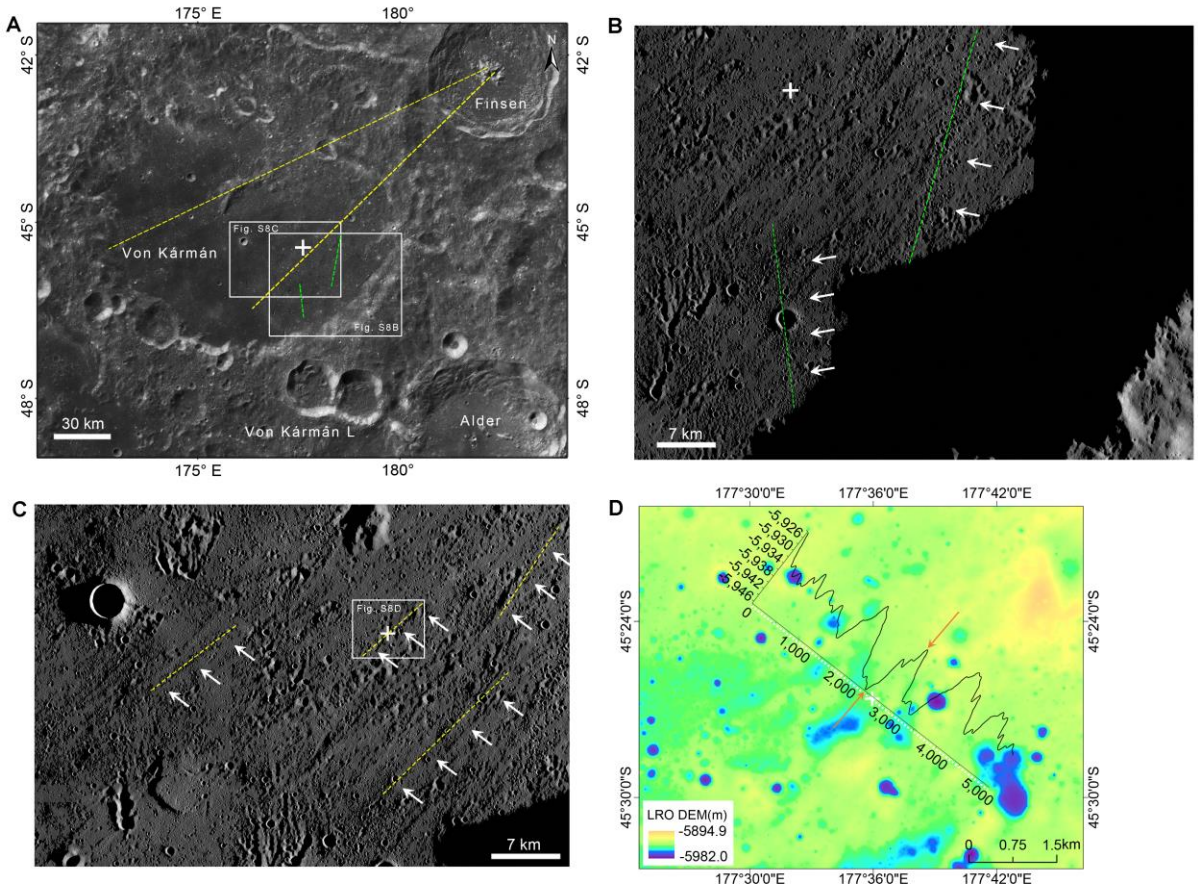

Fig. S8. Geological context and topography at CE-4 landing site. (A) Optical image illustrating the CE-4 landing site, where the yellow and green lines show the directions of ejecta from Finsen and Von Kármán L, respectively. The white cross indicates the CE-4 landing site. **(B)** Kaguya TC images showing the crater chains from Von Kármán L crater and **(C)** from Finsen crater. **(D)** Topographic profile (black line) across a secondary crater chain formed by Finsen crater, showing that the present rim-to-floor depth of the secondary crater (labeled by the red arrows) is >16 m. The base image is the LROC NAC DTM with a resolution of 2 m/pixel.

Table S1. Estimated ejecta thickness at the CE-4 landing site from Finsen, Von Kármán L, and Von Kármán L' craters. Note that several craters have contributed to ejecta deposits at the transverse route of Yutu-2, and here we list only the three nearest source craters. Therefore, the estimated total ejecta thickness should be regarded as the minimum value.

Craters	diameter (km)	Latitude (°)	Longitude (°)	Distance between the crater center and landing site (km)	Estimated ejecta thickness (m) *
Finsen	72.9	-42.29	182.28	140.1	5.9
Von Kármán L	28.8	-47.83	177.90	72.7	1.3
Von Kármán L'	29.6	-48.07	178.98	83.5	1.0
Total ejecta thickness (m)					8.1

*Equation (8) and (9).

Table S2. The data IDs for the images used in the figures.

Figures Number	Data ID
Fig. 1	CE2_GRAS_DOM_07m_J240_38S175E_A.tif (http://moon.bao.ac.cn/cedownload/CCD/IMAGE/DOM/CE2_GRAS_DOM_07m_J240_38S175E_A.tif) CE2_GRAS_DOM_07m_J201_38S175W_A.tif (http://moon.bao.ac.cn/cedownload/CCD/IMAGE/DOM/CE2_GRAS_DOM_07m_J201_38S175W_A.tif) CE2_GRAS_DOM_07m_K101_45S175W_A.tif (http://moon.bao.ac.cn/cedownload/CCD/IMAGE/DOM/CE2_GRAS_DOM_07m_K101_45S175W_A.tif) CE2_GRAS_DOM_07m_K136_45S175E_A.tif (http://moon.bao.ac.cn/cedownload/CCD/IMAGE/DOM/CE2_GRAS_DOM_07m_K136_45S175E_A.tif)
Fig. 2; Fig. S2; Fig. S3B; Fig. S4	CE4_GRAS_LPR-2B_SCI_N_20190104004000_20190109213900_0001_A.2B
	CE4_GRAS_LPR-2B_SCI_N_20190109213901_20190111150200_0002_A.2B
	CE4_GRAS_LPR-2B_SCI_N_20190111150201_20190112102100_0003_A.2B
	CE4_GRAS_LPR-2B_SCI_N_20190131080301_20190201054300_0005_A.2B
	CE4_GRAS_LPR-2B_SCI_N_20190201054301_20190208101200_0006_A.2B
	CE4_GRAS_LPR-2B_SCI_N_20190208101201_20190209053100_0007_A.2B
	CE4_GRAS_LPR-2B_SCI_N_20190209053101_20190209130800_0008_A.2B
	CE4_GRAS_LPR-2B_SCI_N_20190209130801_20190210033400_0009_A.2B
	CE4_GRAS_LPR-2B_SCI_N_20190210033401_20190211100800_0010_A.2B
Fig.2B	CE4_GRAS_LPR_Tomographic-Image.mat (http://moon.bao.ac.cn/searchOrder_Tomographic_Image.search)
Fig. S1	CE4-R_GRAS_9999_PCAM-R_RGB_000_002002_R_20190508023755_A.tif (http://moon.bao.ac.cn/CE4/PCAM/CE4-R_GRAS_9999_PCAM-R_RGB_000_002002_R_20190508023755_A.tif)
Fig. S3A	CE3_BMYK_LPR-2B_SCI_N_20131221124501_20131223174500_0005_A.2B
	CE3_BMYK_LPR-2B_SCI_N_20131223174501_20131226000000_0006_A.2B
	CE3_BMYK_LPR-2B_SCI_N_20131226000001_20140112193800_0007_A.2B
Fig. S7	(A). CE2_GRAS_DOM_07m_K136_45S175E_A.tif (http://moon.bao.ac.cn/cedownload/CCD/IMAGE/DOM/CE2_GRAS_DOM_07m_K136_45S175E_A.tif)
	(B). R: https://astrogeology.usgs.gov/search/map/Moon/Kaguya/MI/MineralMaps/Lunar_Kaguya_MIMap_MineralDeconv_FeOWeightPercent_50N50S G: https://astrogeology.usgs.gov/search/map/Moon/Kaguya/MI/MineralMaps/Lunar_Kaguya_MIMap_MineralDeconv_ClinopyroxenePercent_50N50S

	B: https://astrogeology.usgs.gov/search/map/Moon/Kaguya/MI/MineralMaps/Lunar_Kaguya_MIMap_MineralDeconv_PlagioclasePercent_50N50S
Fig. S8	(A). CE2_GRAS_DOM_07m_J240_38S175E_A.tif (http://moon.bao.ac.cn/cedownload/CCD/IMAGE/DOM/CE2_GRAS_DOM_07m_J240_38S175E_A.tif) CE2_GRAS_DOM_07m_J201_38S175W_A.tif (http://moon.bao.ac.cn/cedownload/CCD/IMAGE/DOM/CE2_GRAS_DOM_07m_J201_38S175W_A.tif) CE2_GRAS_DOM_07m_K101_45S175W_A.tif (http://moon.bao.ac.cn/cedownload/CCD/IMAGE/DOM/CE2_GRAS_DOM_07m_K101_45S175W_A.tif) CE2_GRAS_DOM_07m_K136_45S175E_A.tif (http://moon.bao.ac.cn/cedownload/CCD/IMAGE/DOM/CE2_GRAS_DOM_07m_K136_45S175E_A.tif)
	(B). TCO_MAPm04_S45E174S48E177SC.IMG (https://darts.isas.jaxa.jp/pub/pds3/sln-l-tc-5-morning-map-v4.0/lon174/data/TCO_MAPm04_S45E174S48E177SC.img) TCO_MAPm04_S45E177S48E180SC.IMG (https://darts.isas.jaxa.jp/pub/pds3/sln-l-tc-5-morning-map-v4.0/lon177/data/TCO_MAPm04_S45E177S48E180SC.img)
	(C). TCO_MAPm04_S45E174S48E177SC.IMG (https://darts.isas.jaxa.jp/pub/pds3/sln-l-tc-5-morning-map-v4.0/lon174/data/TCO_MAPm04_S45E174S48E177SC.img) TCO_MAPm04_S45E177S48E180SC.IMG (https://darts.isas.jaxa.jp/pub/pds3/sln-l-tc-5-morning-map-v4.0/lon177/data/TCO_MAPm04_S45E177S48E180SC.img)
	(D). NAC_DTM_CHANGE4_E458S1775.IMG (http://lroc.sese.asu.edu/data/LRO-L-LROC-5-RDR-V1.0/LROLRC_2001/DATA/SDP/NAC_DTM/CHANGE4/NAC_DTM_CHANGE4_E458S1775.IMG)